



Assessment of Primary Slice Release Residual Stress Mapping in a Range of Specimen Types

M.D. Olson¹  · A.T. DeWald¹ · M.R. Hill²

Received: 22 January 2018 / Accepted: 17 July 2018 / Published online: 29 August 2018
© Society for Experimental Mechanics 2018

Abstract

This paper further explores the primary slice removal technique for planar mapping of multiple components of residual stress and describes application to specimens with a range of alloys, geometries, and stress distributions. Primary slice release (PSR) mapping is a combination of contour and slitting measurements that relies on decomposing the stress in a specimen into the stress remaining in a thin slice and the stress released when the slice is removed from a larger body. An initial contour method measurement determines a map of the out-of-plane stress on a plane of interest. Subsequently, removal of thin slices and a series of slitting measurements determines a map of one or both in-plane stress components. Four PSR biaxial mapping measurements were performed using an aluminum T-section, a stainless steel plate with a dissimilar metal slot-filled weld, a titanium plate with an electron beam slot-filled weld, and a nickel disk forging. Each PSR mapping measurement described herein has one (or more) complementary validation measurement to confirm the technique. Uncertainty estimates are included for both the PSR mapping measurements and the validation measurements. Agreement was found between the PSR mapping measurements and validation measurements showing that PSR mapping is a viable technique for measuring residual stress fields.

Keywords Residual stress · Measurement · Primary slice release · Contour method · Slitting

Introduction

A wide variety of experimental techniques are available to determine residual stress, and technique selection is an important consideration for engineering work. Any residual stress measurement technique provides only a subset of the full stress tensor over a limited spatial volume on a given specimen [1]. Very few measurement techniques can determine a 2D map of multiple components of residual stress on a plane through the workpiece. Neutron diffraction and high-energy X-ray diffraction are capable of measuring maps of multiple components of bulk residual stress. Both diffraction techniques are viable for many specimen types, but measurements can be difficult for

parts of large size, or for materials with large grains or high levels of microstructural texture. A superposition of multiple techniques can also be used to map multiple stress components; however this can be challenging, and requires a diverse skill set.

The use of the contour method [2] in conjunction with other methods has proven fruitful, since the contour method provides a complete 2D map of the residual stress component normal to a plane of interest. In recent work, a second measurement technique is used to map a second stress component on the same plane, using a series of repeated point or line measurements. The first example of using the contour method and another method (hole drilling and x-ray diffraction) was provided in [3], and that approach was subsequently applied to a girth welded mock-up [4], as well as several additional specimen types [5–8]. Another biaxial mapping approach combined the contour method with incremental slitting [9] and is called primary slice removal (PSR) mapping. An advantage of PSR mapping is that the in-plane stress can be mapped with relatively few measurements and additionally PSR mapping takes advantage of the high precision offered by slitting [10–12]. PSR mapping was first demonstrated on a quenched aluminum extrusion [9] and was

✉ M. D. Olson
molson@hill-engineering.com

¹ Hill Engineering, LLC, 3083 Gold Canal Drive, Rancho Cordova, CA, USA

² Department of Mechanical and Aerospace Engineering, University of California, Davis, One Shields Avenue, Davis, CA, USA



subsequently applied to map biaxial residual stresses in a stainless steel welded plate [13] and a complex nuclear power plant nozzle mockup containing a dissimilar metal weld [14]. PSR mapping was recently applied to measure three orthogonal residual stress components in a quenched aluminum bar and was validated with complementary measurements by neutron diffraction [15].

The primary objective of the present study is to assess the PSR mapping approach in specimens that encompass a range of key industrial alloys, geometries, and stress distributions. This work therefore complements the prior publications that laid out in detail the PSR mapping technique [9] or described its application to specific problems [13–15].

Methods

PSR mapping measurements were performed on four different specimen types: an aluminum T-section, a stainless steel plate with a dissimilar metal (DM) slot-filled weld, a titanium plate with an electron beam (EB) slot-filled weld, and a nickel alloy forging. Validation was performed by comparing results of PSR mapping to complementary measurements. The following is a description of the methods used for these experiments.

Primary Slice Removal (PSR) Mapping

PSR mapping is a measurement approach that combines the contour method and slitting to determine multiple components of residual stress [9]. The measurement determines the stress field at a given measurement plane, in the original specimen configuration. The basic steps for PSR mapping measurements are shown in Fig. 1. First, the contour method is used to measure the residual stress normal to a plane of interest, near to the mid-length of the specimen. Next, a thin slice (or multiple slices) adjacent to the contour method measurement plane is removed. During slice removal, the residual stress will change by an amount called the PSR stress. The stress remaining in the removed thin slice, referred to as the *slice stress*, is determined using

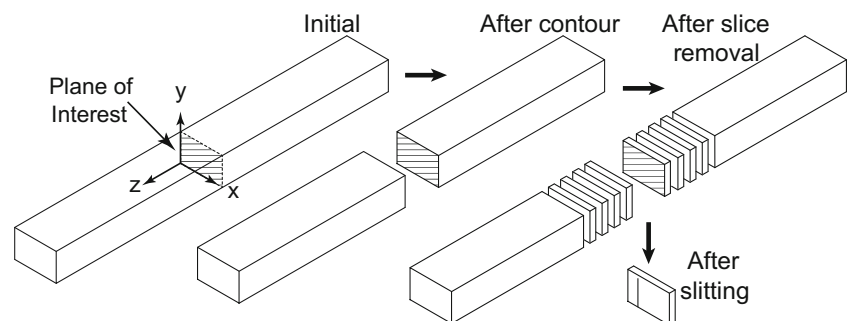
a series of slitting measurements. By invoking elastic superposition, the stress in the original configuration is expressed as the sum of the slice stress (remaining in the removed thin slice) and the PSR stress (the stress released when the slice is removed from the body). Previous work [9, 16] has shown that three orthogonal components of the PSR stress can be computed in a supplementary stress analysis that uses as input the out-of-plane stress determined from the contour method measurement. A fuller description of PSR mapping was provide earlier [9].

Contour method measurements

The contour method is a residual stress measurement technique invented by Prime [2]. A contour method measurement cuts a workpiece along a given measurement plane. Residual stress release causes the cut surfaces to deform in a manner analogous to the pre-cut residual stress field. The cut surface profiles can be measured, and their negative (mirror image) applied as a displacement boundary condition in an elastic stress analysis of the cut part, which determines the residual stress normal to the cutting plane. Prime and DeWald [17] describe the theory, experimental steps, and best practices for the contour method.

The contour method measurements for each PSR mapping measurement followed nominally the same procedure. For each contour method measurement, the specimen was cut in two using a wire electric discharge machine (EDM) while the specimen was rigidly clamped to the EDM frame. Following cutting, the profile of each of the two opposing cut faces was measured with a laser scanning profilometer to determine the surface height normal to the cut plane as a function of in-plane position. Surface height data were taken on a grid of points with spacing between 100 and 200 μm in two orthogonal in-plane directions. The data for the two cut surface profiles were then aligned, averaged on a common grid, and the average was fit to a smooth bivariate analytical function. The residual stress release on each measurement plane was found by applying the negative of the smoothed surface profile as a boundary condition on the cut face of a linear elastic finite element

Fig. 1 Experimental steps used in a PSR mapping measurement



model of the cut part. Each model used the corresponding elastic material properties given in Table 1.

Primary slice removal stress

The PSR stress, which is the stress released from the slice as it is extracted from the body, is determined using a supplemental finite element analysis [9]. The analysis uses a model of the slice and applies the out-of-plane stress (measured with the contour method) as a traction boundary condition on the slice faces. The resulting stress after equilibrium gives the PSR stress. Further validation for the PSR method is provided in [5, 14].

Slitting measurements

Slitting was used to determine the stress remaining in the removed slice. Each slitting measurement incrementally cut a slit into the slice. During cutting, strain was recorded using a bonded strain gage on the back face of the slitting measurement plane. The strain versus cut depth data in conjunction with an elastic inverse (*compliance matrix*) is used to calculate the stress released while cutting the incremental slit. A unique compliance matrix that reflected the geometry of slice while it was being slit was used for each measurement. The stress calculation procedure reduces the effect of noise in the strain data with Tikhonov regularization [18]. Hill [19] provided a useful summary of the slitting method, including details of theory and application.

Uncertainty estimation

The uncertainty for the contour method measurements was estimated using the approach developed in [20] and further evaluated in [21]. The contour method uncertainty estimate consists of two random uncertainty sources and they are the uncertainty due to noise in the displacement surfaces (“*displacement error*”) and the uncertainty arising from smoothing of the displacement surfaces (“*model error*”). The displacement error is estimated using a Monte Carlo approach by finding the standard deviation of the differences in

stress resulting from applying normally distributed noise to the measured surface and the model error was found by taking the standard deviation of stresses computed using different levels of smoothing.

The uncertainty in the slitting measurements was calculated using the difference between the smoothed strain and measured strain (or alternately with an assumed, omnipresent value of $2 \mu\epsilon$) in the stress calculation procedure.

All uncertainty in the PSR stress is assumed due to uncertainty from the contour method measurement and uncertainty in the in-plane components of the PSR stress was assumed to be negligible based on prior work [9], where it was found that the smooth out-of-plane stress field causes an in-plane stress field robust to small-scale, random variations in the out-of-plane stress. As a result, uncertainty in the total in-plane stress components derives entirely from uncertainty in the slitting measurements and uncertainty in the total out-of-plane stress component derives entirely from uncertainty in the contour measurement.

Geometry and Material

A range of specimens was developed and PSR mapping was performed on each. The specimens and measurement details are described below. Complementary validation measurements are also described.

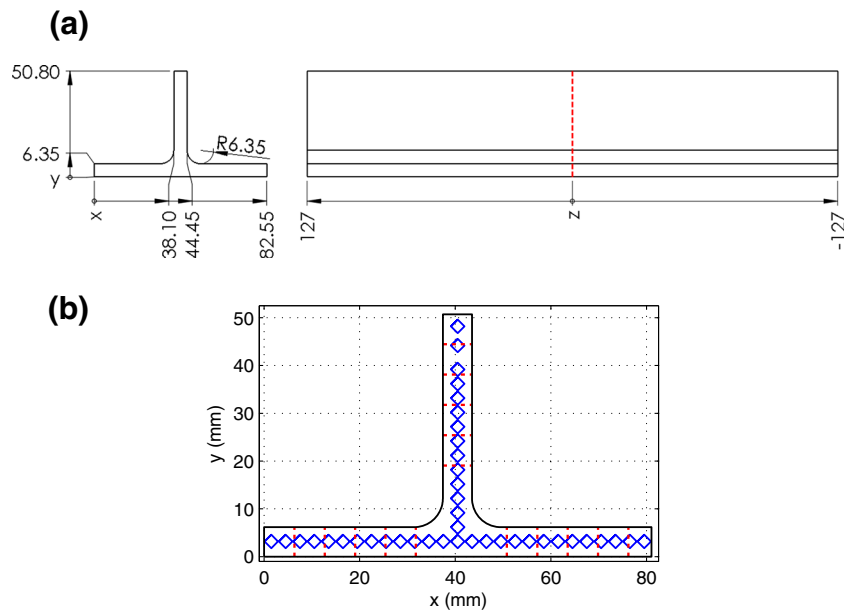
Aluminum T-section

The aluminum T-section specimen was fabricated from a bar cut from 82.5 mm (3.25 in) thick 7050-T7451 aluminum plate. The bar had a length of 762 mm (30.0 in), a height of 82.5 mm (3.25 in), and a width of 82.5 mm (3.25 in). The bar was heat treated, including a quench, to induce high residual stress indicative of the -T74 temper. The heat treatment is described in [22] and consists of heating the bar to 477 °C (890 °F) for 3 h, quenching in room temperature water, artificial aging at 121 °C (250 °F) for 8 h followed by additional aging at 177 °C (350 °F) for 8 h. The T-section specimen machined from the bar had a length of 254 mm (10.0 in), a height of 50.8 mm (2.0 in),

Table 1 Material properties for each of the specimens

Specimen	Elastic Modulus (GPa)	Poisson's Ratio	Yield Strength (MPa)
Aluminum T-section (7050-T7451)	71	0.33	460
Titanium EB welded plate (Ti-6Al-4V)	110	0.31	960
Nickel forging (Udimet-720Li)	200	0.31	300–500
Stainless steel DM welded plate (316 L plate)	203	0.3	440
Stainless steel DM welded plate (A52 weld)	211	0.289	345–482

Fig. 2 Aluminum T-section (a) dimensions and PSR measurement location ($z = 0$) and (b) slitting (red lines) and neutron diffraction (blue diamonds) measurement locations (dimensions in mm)



a width of 82.55 mm (3.25 in), and a leg thicknesses of 6.35 mm (0.25 in), as shown in Fig. 2. The PSR mapping measurement plane was at the specimen mid-length, 127 mm (5 in) from each end, as shown in Fig. 2. Two 6.35 mm (0.25 in) thick, prismatic slices were removed adjacent to the measurement plane. The stresses remaining in the slices was determined with slitting at the measurement locations shown in Fig. 2.

Stainless steel DM welded plate

The stainless steel dissimilar metal (DM) weld specimen was fabricated from a high-strength 316 L stainless steel plate. The plate had a 25.4 mm (1.0 in) by 152.4 mm (6.0 in) cross-section and a length of 1.22 m (48.0 in). A slot was machined along the entire length of the plate with a depth of 9.53 mm (0.375 in), a width of 19.05 mm (0.75 in), and a 70° root angle. The slot and plate cross-section can be seen in Fig. 3. Prior to filling the slot with weld material, the plate was constrained by welding the plate to an additional support plate. The weld joining the plate to the support plate was a continuous 7.94 mm (0.313 in) fillet weld that was applied along both 1.22 m edges of the plate. The slot weld was made using eight passes, each continuous along the entire length of the plate using an automated welder. Gas tungsten arc welding (GTAW) was used to fill the slot with 0.89 mm (0.035 in) diameter A52M (ERNiCrFe-7A) wire. The relevant welding parameters are: 250 A current, 10.5 V voltage, and 101.6 mm/min (4 in/min) travel speed. This specimen is similar to a stainless steel weld studied earlier [13], but here the nickel alloy weld metal is used to reflect DM welds found in nuclear electric pressurized water reactor piping.

Following welding, the fillet welds were machined away to release the DM welded plate from the support plate and the ends of the DM welded plate were removed (by saw cut) to eliminate the inconsistent weld bead geometry at the start and stop of the weld. The remaining section was 1.02 m (40.0 in) long and the measurement plane was at the plate mid-length. Two 6.35 mm (0.25 in) thick slices were removed adjacent to the measurement plane. The slitting measurements in the slices were made at the locations shown in Fig. 3.

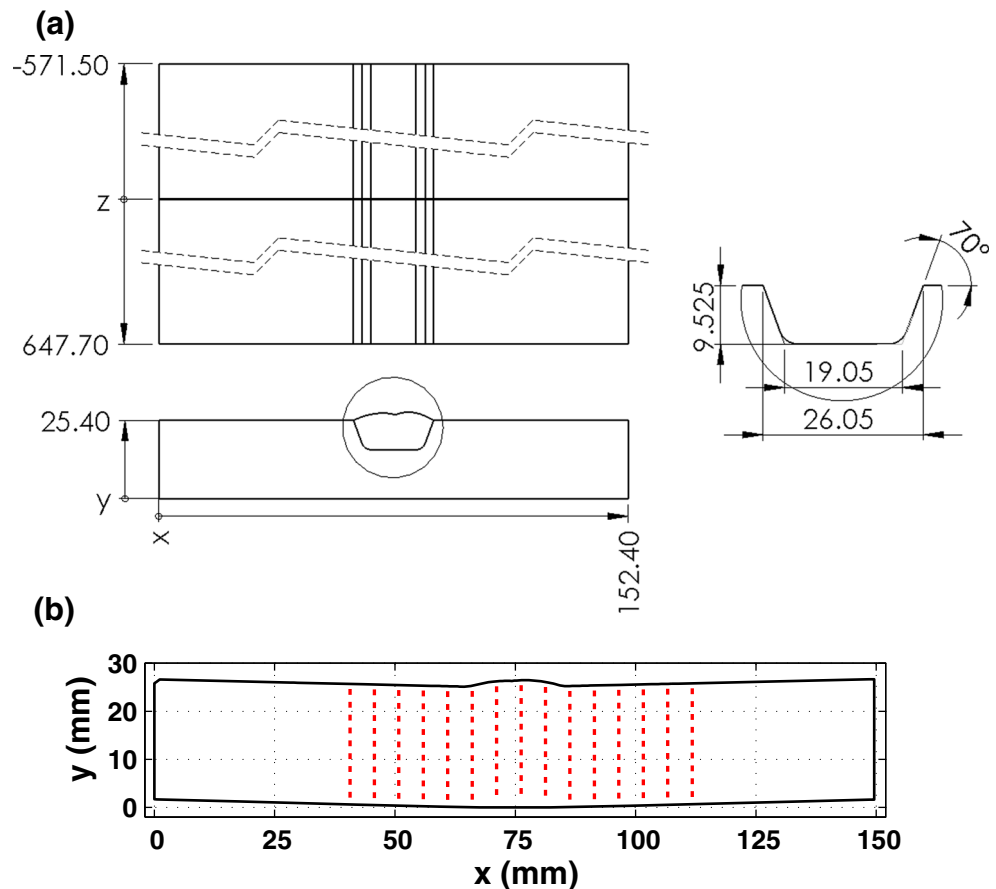
Titanium electron beam welded plate

The titanium alloy electron beam (EB) welded plate specimen was fabricated using one long Ti-6Al-4V plate, with similar geometry to the stainless steel DM welded plate (same cross-section and slot dimensions). The weld process is a typical wire-fed additive manufacturing process, but service parts would typically be subjected to thermal stress relief following welding. The groove was filled along the entire length of the plate with 8-passes of 3.18 mm (0.125 in) diameter Ti-6Al-4V wire. After completion of the weld, the plate was sectioned into 101.6 mm (4.0 in) long pieces, as shown in Fig. 4. The measurement plane was at the plate mid-length, as shown in Fig. 4. Both the slice removal and the slitting measurement locations in the titanium alloy electron beam (EB) welded plate specimen were identical to those for the stainless steel DM welded plate specimen, as in Fig. 4(b).

Nickel alloy forging

The nickel alloy (Udimet-720Li) forging specimen is representative of a small turbine disk forging and has a diameter of

Fig. 3 Stainless steel dissimilar metal weld (a) dimensions and PSR measurement location ($z = 0$) and (b) slitting measurement locations (dimensions in mm)



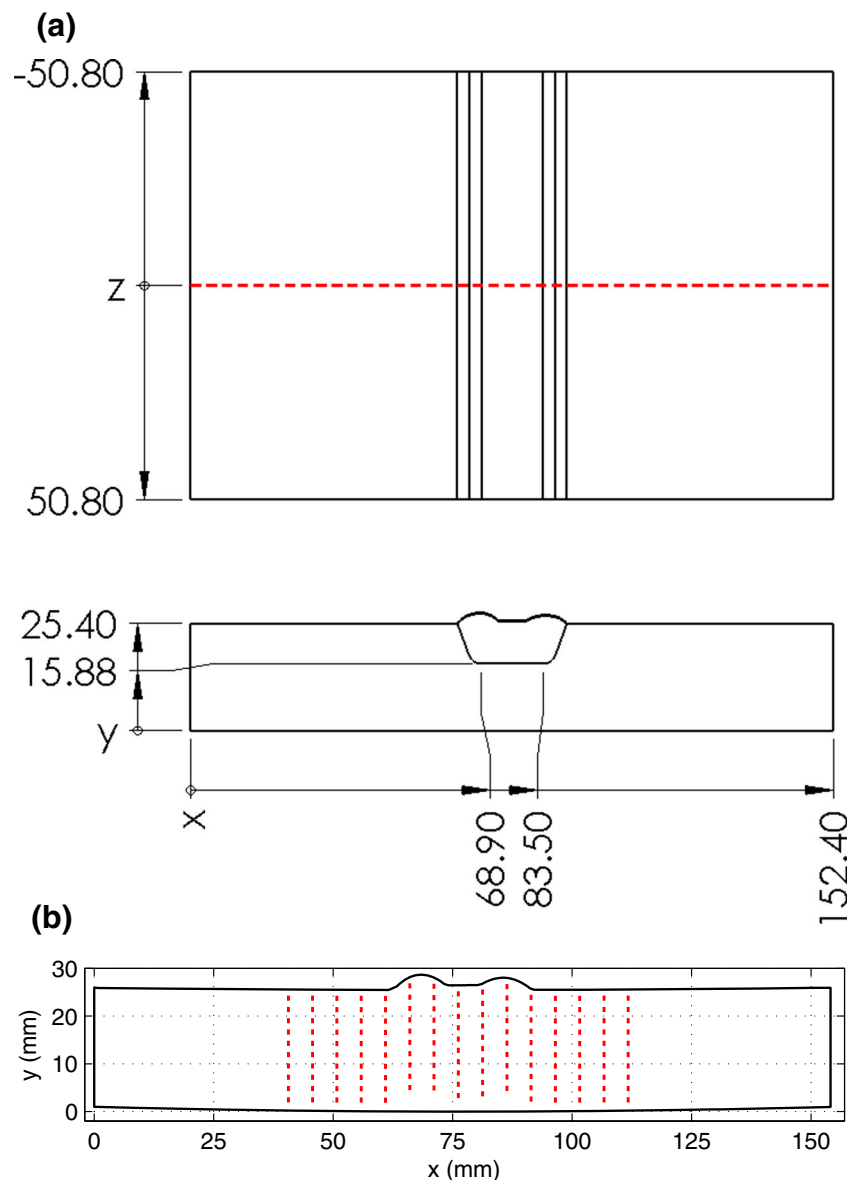
151.20 mm (5.95 in) and a maximum height of 70.41 mm (2.77 in), as is shown in Fig. 5. The specimen was forged and heat treated, including a quench, to achieve desired mechanical properties. The heat treatment consisted of pre-heating the specimens to 1080 °C (1975 °F), forging to the nominally finished shape, solution heat treating at 1105 °C (2020 °F), and oil quenching. The specimen was then stabilized at 760 °C (1400 °F) for 8 h, air cooled, aged at 650 °C (1200 °F) for 24 h and then air cooled to room temperature. Prior to measurement, the specimen was sectioned in half to leave two 180 degree half forgings. Strain change was measured during the sectioning operation using strain gages at multiple locations, and was used in an additional stress analysis to compute the stress change. The stress analysis consisted of applying a bending moment to the sectioned face of the specimen and extracting the resulting strain at the strain gage locations. The simulated strain (multiplied by a scaling factor) was then fit to the measured strain data. The simulated strain fit the measured strain well and the effect of the scaled bending moment stress distribution on the subsequent measurement plane gives the release stress when the specimen was sectioned. The measurement plane was at the specimen mid-width (shown in Fig. 5) and the reported results include the stress released by sectioning.

Three wedge shaped slices were removed adjacent to the measurement plane and were 6.35 mm thick at the slice mid-length. Due to the geometry of the slice, the slices were bisected with a contour method measurement at $y = 35.2$ mm (1.386 in). Reported slice stresses include the effect of this contour method measurement. The effect of the contour method measurement was determined using the approached developed by Wong and Hill [23], which consists of extracting stress release from the previous contour method measurement at the location of the subsequent measurement(s). The slitting measurements were made at the locations shown in Fig. 5(b).

Validation Measurements

Each of the four PSR mapping measurements were accompanied by an additional measurement, in a replicate specimen, to validate the PSR mapping approach. The validation measurements for the aluminum T-section, stainless steel DM welded plate, and the titanium EB welded plate were performed using the slitting method. The validation measurements in the nickel alloy forging used the contour method. Additionally, neutron diffraction validation measurements were performed in the aluminum T-section. The validation measurements will be compared with the PSR maps.

Fig. 4 Titanium electron beam welded plate (a) dimensions and PSR measurement location ($z = 0$) and (b) slitting measurement locations (dimensions in mm)



Aluminum T-section

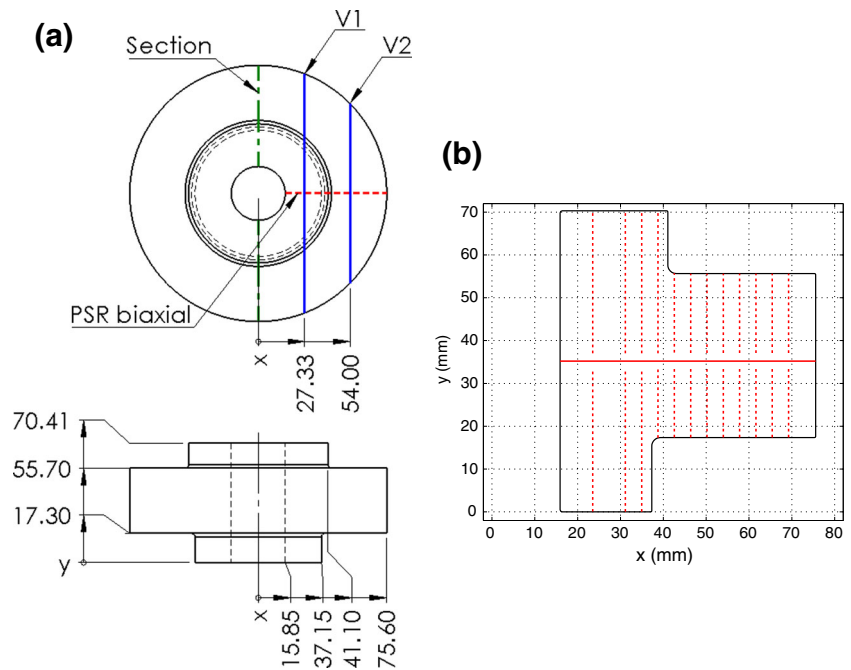
Validation measurements for the aluminum T-section used neutron diffraction. The neutron diffraction measurements were performed at the Neutron Diffraction Stress Mapping Facility (NRSF2) at the High-Flux Isotope Reactor (HFIR) at Oak Ridge National Laboratory. NRSF2 is a monochromatic beam diffractometer that uses a 1.73 \AA incoming neutron wavelength.

The neutron diffraction measurements used standard methodologies [24] and consisted of collecting interatomic lattice spacing data (d) in a specimen containing residual stress and lattice spacing data in a stress-free specimen (d_0) for three orthogonal directions, and then computing strain and stress [25]. The specimen containing residual stress,

used to measure d , was a separate, but nominally identical T-section specimen used in the PSR mapping measurement. The stress-free specimens, used to measure d_0 , consisted of a series of cubes with an edge length of 3.0 mm that were removed adjacent to the PSR mapping measurement plane. Eleven cubes were removed using wire electric discharge machining (EDM).

Measurements in the d specimens were made along one horizontal line at $y = 3.175 \text{ mm}$ (bottom flange mid-height) and one vertical line at $x = 40.52 \text{ mm}$ (central flange mid-width). Measurements were made at $x = 1.52$ to 79.52 mm in increments of 3.0 mm for the horizontal line and $y = 3.18$ to 48.18 mm in increments of 3.0 mm for the vertical line, as shown in Fig. 2(b). Lattice spacings were found for the $311 \{hkl\}$ lattice plane and used a gage volume of $2 \text{ mm} \times$

Fig. 5 Nickel disk forging (a) dimensions and measurement locations (dashed red line for PSR mapping measurement and solid blue lines for validation contour measurement locations) and (b) slice measurement locations (slitting measurement locations (dashed lines) and contour location (solid line)) (dimensions in mm)



2 mm for the x and y -directions (in-plane directions) and 20 mm along the z -direction (specimen length direction). Uncertainty was calculated by propagating the lattice spacing uncertainty through the equations for strain and stress. The material properties used in the stress calculation, $E_{\{311\}}$ and $\nu_{\{311\}}$, were assumed to be the same as the bulk material properties given in Table 1.

Stainless steel DM welded plate

The validation slitting measurements in the stainless steel DM welded plate consisted of one slitting measurement of σ_{xx} at $x = 76.2$ mm. The specimen used for the validation measurement was a 127 mm (5 in) long specimen that was removed from the 1.22 m (48.0 in) long plate that was used in the PSR mapping measurements.

Titanium electron beam welded plate

The validation slitting measurement in the titanium EB welded plate consisted of one slitting measurement of σ_{xx} at $x = 68.15$ mm (center of one of the weld pass crowns). The specimen was cut from the same plate and nominally identical to the one used for the PSR mapping measurements.

Nickel alloy forging

The validation measurements for the nickel forging consisted of contour method measurements of σ_{xx} at $x = 27.33$ and 54.0 mm as shown in Fig. 5. The validation measurement used a separate specimen, nominally identical to the one used for

the PSR mapping measurements that was not previously sectioned in half. The measurement at $x = 27.33$ mm was performed first and the results at the second measurement location ($x = 54.0$ mm) include the effects of stress release from the first measurement at $x = 27.33$ mm. The disk is assumed to be axisymmetric, so that the PSR mapping measurement (σ_{zz}) can be compared with the validation measurement (σ_{xx}) only on the plane of interest.

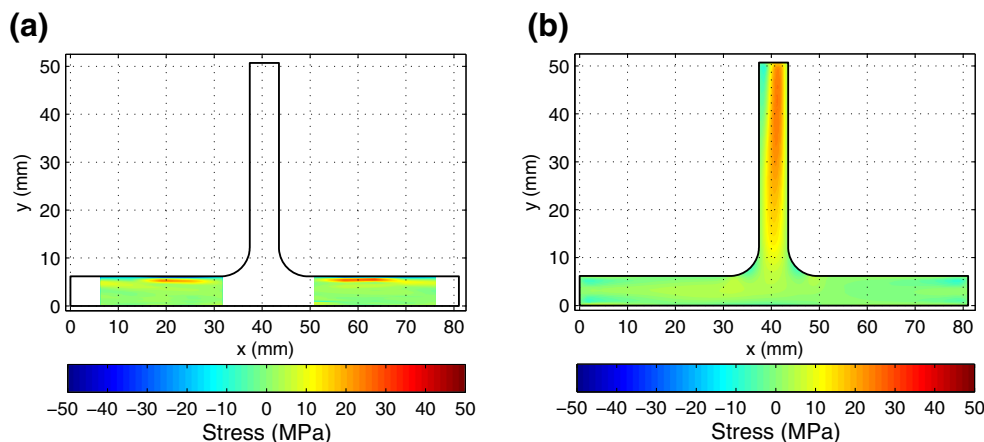
Results

Results for each of the four specimen types are summarized in Figs. 6 through 21. For each specimen type the following results are shown: 1) a fringe plot of the stress released due to removing the slice from the body (i.e., PSR stress), 2) the measured residual stress remaining in the thin slice (i.e., the slice stress), 3) total stress (i.e., stress in the initial configuration = 1 + 2) and uncertainties, and 4) line plots comparing the PSR mapping measurement and the validation measurement.

Aluminum T-Section

The long-transverse slice stress (σ_{xx}) in the aluminum T-section has near zero residual stresses at most points and with larger tensile stresses near the upper portion of the bottom flange (50 MPa) and significant compressive stresses at the top of the bottom flange (−125 MPa). The long-transverse PSR stress is nominally near zero along the entire bottom

Fig. 6 Measured x-direction (a) stress and (b) PSR stress in a thin slice from the aluminum T-section specimen



flange (where the long-transverse slice stresses were measured) (Fig. 6).

The short-transverse slice stress (σ_{yy}) in the aluminum T-section has low magnitude residual stress at most points and with slightly larger magnitude compressive stresses near the left and right edges of the central flange (-30 MPa). The short-transverse PSR stress has low magnitude near the edges of the central flange and larger tensile stresses at the middle of the central flange (20 MPa) (Fig. 7).

The total stress and uncertainty maps are shown in Fig. 8. The longitudinal stress (σ_{zz}), as measured using the contour method, has compressive stress at the left and right edges of the bottom flange ($\min \approx -240$ MPa) and at the top of the center flange (≈ -70 MPa) with tensile stress at the intersection of the bottom and center flanges ($\max \approx 100$ MPa). The long-transverse stress (σ_{xx}) has essentially the same distribution as the PSR stress with most points having low magnitude stress and larger tensile stresses near the upper portion of the bottom flange (50 MPa) and significant compressive stresses at the top of the bottom flange (-125 MPa). The short-transverse stress (σ_{yy}) has

a distribution that is primarily driven by the PSR stress and has low magnitude near the edges of the central flange and larger tensile stresses at the middle of the central flange (20 MPa). The uncertainty for both the long and short-transverse stress is low at most points, with the largest uncertainties near 10 MPa.

The validation neutron diffraction measurements are shown in the line plots of Fig. 9. The results show that there is excellent agreement between the contour method and neutron diffraction measurements, which are in statistical agreement at nearly every measurement point. However, the neutron diffraction measurement results do have somewhat systematically larger magnitudes than the contour method measurement. This may be due to differences between the bulk and orientation-specific (i.e., $\{311\}$) elastic properties, which were assumed to be identical in the present work.

Stainless Steel DM Welded Plate

The long-transverse slice stress (σ_{xx}) in the stainless steel DM welded plate has low magnitude residual stresses away

Fig. 7 Measured y-direction (a) stress in a thin slice and (b) PSR stress for the aluminum T-section specimen

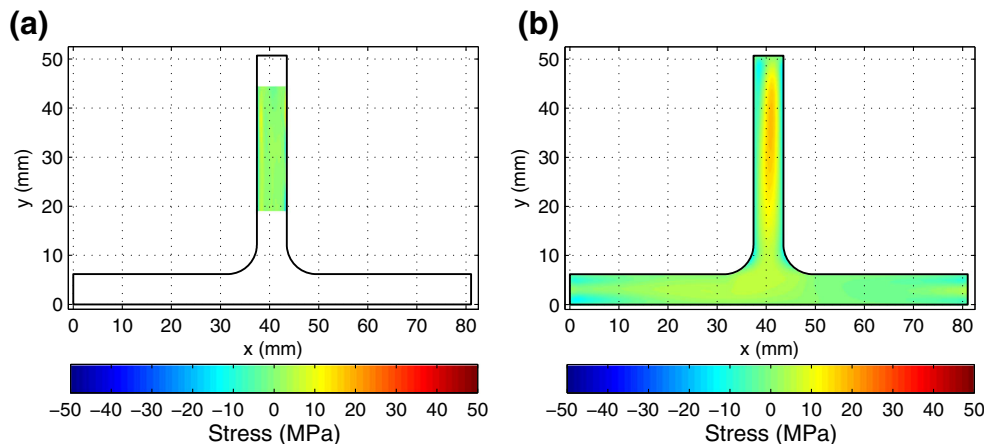
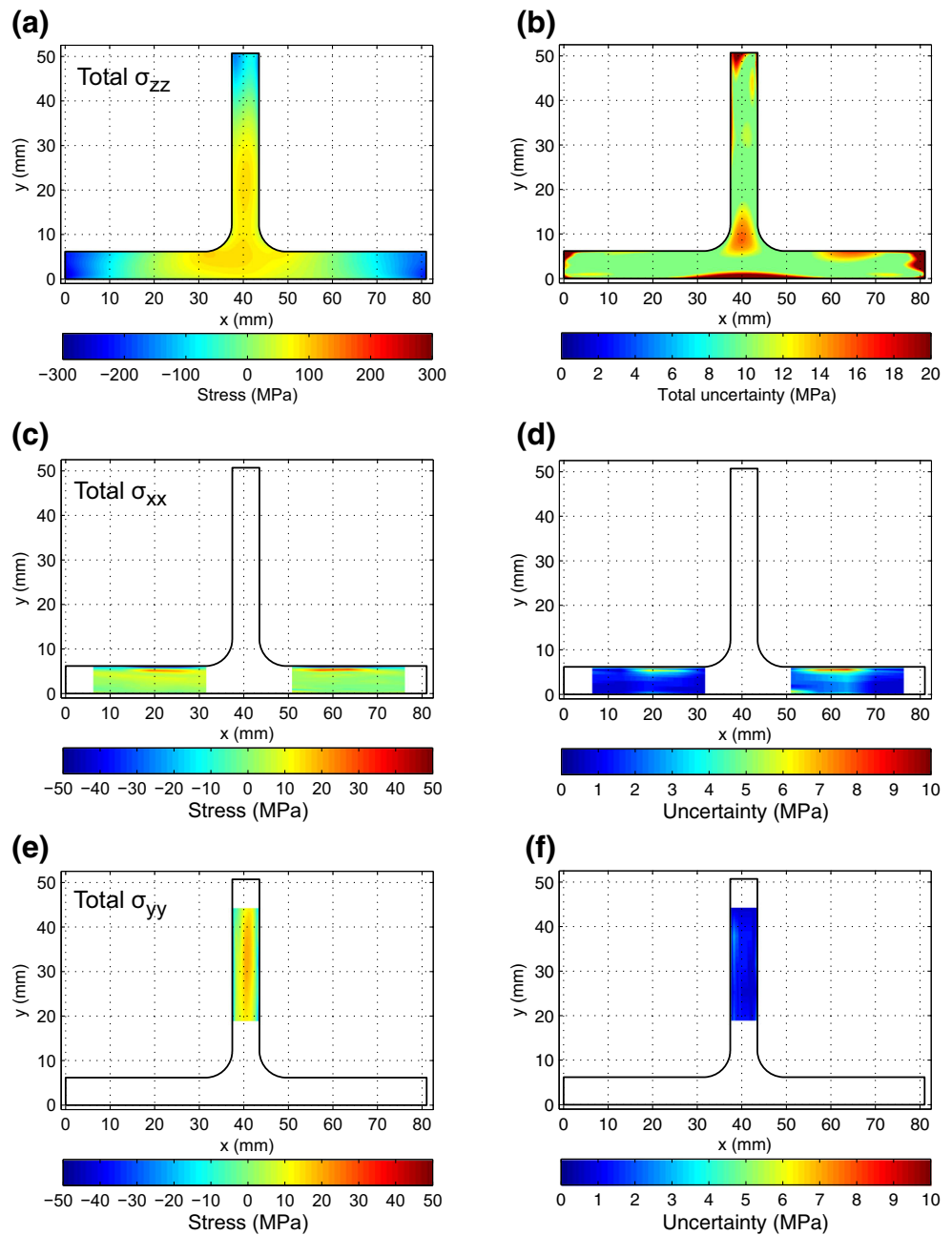


Fig. 8 Stress and uncertainty for the aluminum T-section specimens: **(a)** z-direction stress, **(b)** z-direction uncertainty, **(c)** x-direction stress, **(d)** x-direction uncertainty, **(e)** y-direction stress and **(f)** y-direction uncertainty. Note: Sub-figures use different color scales



from the welded area, significant tensile stress at the weld root (225 MPa), and significant compressive stress toward the bottom of the plate (−150 MPa). The PSR stress is significantly smaller than the slice stress, but also has significant compressive stress at the weld root (75 MPa) and nominally low magnitude stress over the rest of the heat affected zone (Fig. 10).

The total stress and uncertainty maps are shown in Fig. 11. The total longitudinal stress (σ_{zz}) in the stainless steel DM welded plate has tensile stress in the weld area and heat-affected zone (max ≈ 380 MPa) and near $y = 0$ at the left and

right edges of the plate where the plate was tack welded (max ≈ 400 MPa). There is compensating compressive stress toward the top of the plate at the left and right edges (min ≈ -260 MPa). The total long-transverse stress (σ_{xx}) has a very similar distribution to that for the slice stress, with low magnitude residual stresses away from the welded area, significant tensile stress at the weld root (300 MPa), and significant compressive stress toward the bottom of the plate (−150 MPa). The long-transverse stress uncertainty is low away from the weld, but significantly larger between $x = 75$ and 90 mm, with the largest uncertainties near 15 MPa.

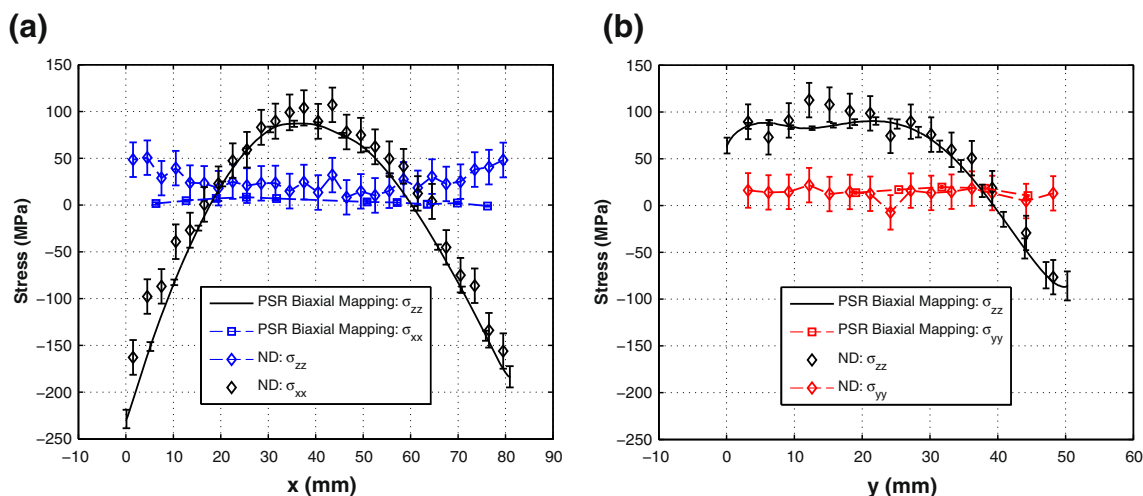


Fig. 9 Line plots of the PSR mapping and neutron diffraction (ND) results along the (a) x-direction at $y = 3.18$ mm for σ_{xx} and σ_{zz} and (b) along the y-direction at $x = 40.52$ mm for σ_{yy} and σ_{zz}

The validation slitting measurement is shown in the line plot of Fig. 12(b). There is excellent agreement between the total PSR mapping results and the validation slitting measurement, with agreement within 10 MPa at most points. However, between $y = 5$ to 10 mm, there is a 40 MPa difference, where the validation measurement shows larger magnitude compressive stress.

Titanium Electron Beam Welded Plate

The long-transverse slice stress (σ_{xx}) in the titanium EB welded plate is similar to the stresses in the stainless steel DM welded plate, with low magnitude away from the

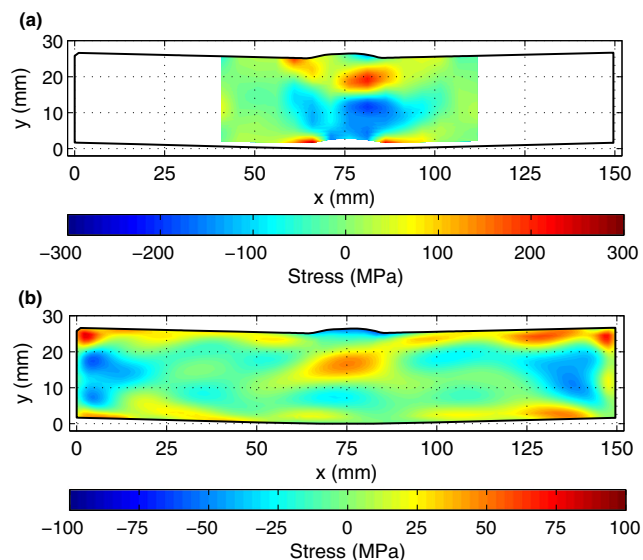


Fig. 10 Measured x-direction (a) stress in a thin slice and (b) PSR stress for the stainless steel DM welded specimen. Note: (a) and (b) use different color scales

welded area, significant tensile stress at the weld root (225 MPa) and towards the bottom of the plate (100 MPa), and significant compressive stress below the weld root (slot bottom) (−200 MPa). The PSR stress is significantly smaller than the slice stress, but has tensile stress at the weld root (75 MPa) and compressive stress below the weld root and at the top of the plate (−50 MPa) (Fig. 13).

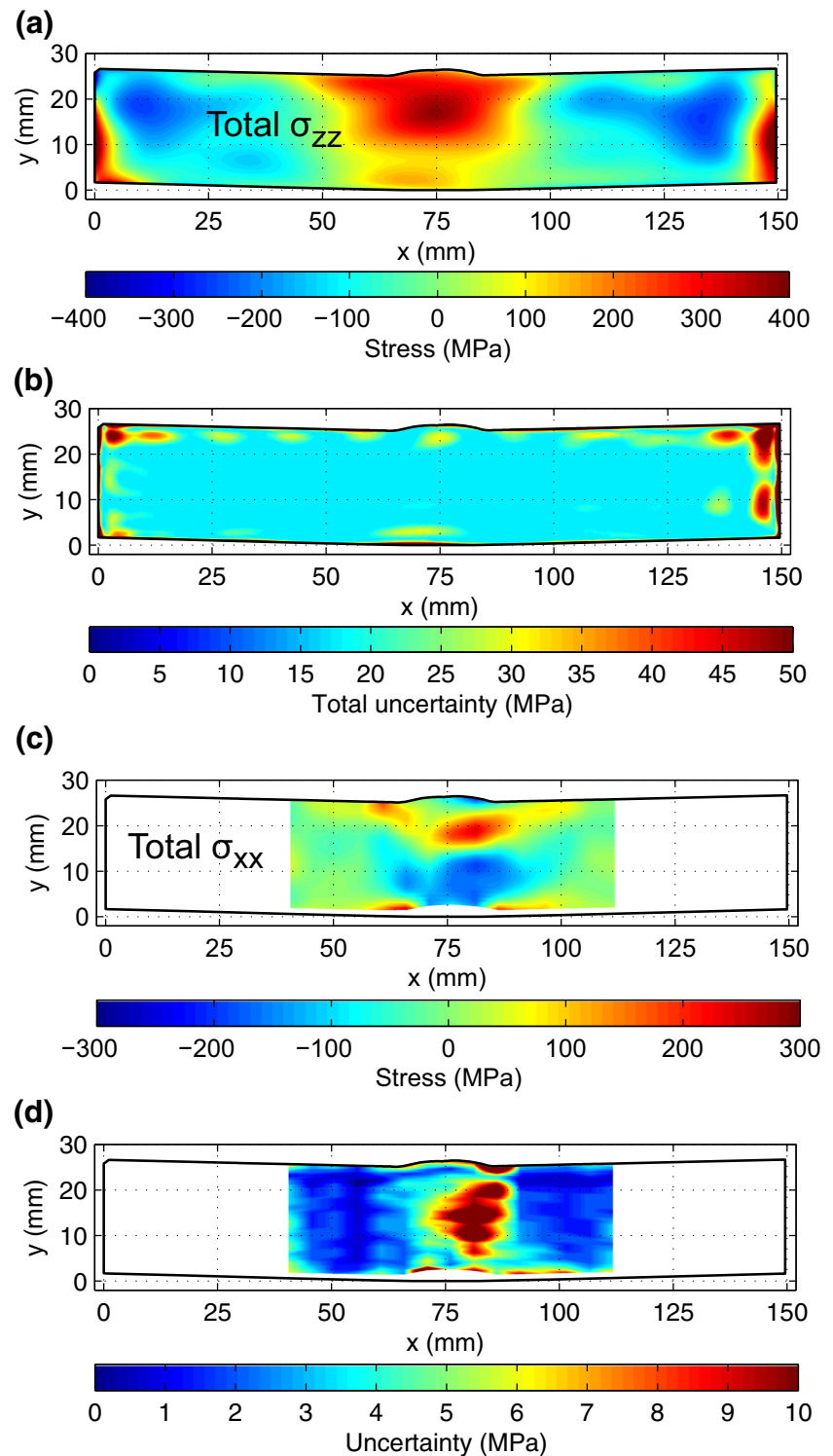
The total stress and uncertainty maps are shown in Fig. 14. The longitudinal stress (σ_{zz}) has tensile stress in the weld area (max ≈ 350 MPa) and compensating compressive stress in the heat-affected zone (min ≈ -200 MPa). The long-transverse stress (σ_{xx}) has a very similar distribution to the slice stress with low magnitude residual stresses away from the welded area, significant tensile stress at the weld root (300 MPa), and significant compressive stress toward the plate mid-height (−250 MPa). The long-transverse stress uncertainty is low away from the weld, but significantly larger between $x = 60$ and 90 mm, with the largest uncertainties near 25 MPa.

The validation slitting measurement is shown in the line plot of Fig. 15(b). As was the case with the stainless steel DM welded plate, there is excellent agreement between the PSR mapping results and the validation slitting measurement, with values within 10 MPa at most points.

Nickel Forging

The radial slice stress (σ_{xx}) in the nickel forging has tensile residual stress toward the center of the forging (75 MPa) and large magnitude compressive stress at the top and bottom of the forging (−250 MPa). The PSR stress also has tensile residual stresses toward the forging center (75 MPa) and compressive stress at the top and bottom of

Fig. 11 Stress and uncertainty for the stainless steel DM welded specimen: (a) z-direction stress, (b) z-direction uncertainty, (c) x-direction stress, and (d) x-direction uncertainty. Note: Sub-figures use different color scales



the forging (-200 MPa). The section release stress change when sectioning the nickel disk forging specimen into half disks has tensile stress in the interior of the sample (130 MPa) and near zero stress at the ID and OD (less than 10 MPa) (Fig. 16).

The hoop stress (σ_{zz}) measured with the contour method (Fig. 17(a)) is tensile towards the center of the forging (max ≈ 200 MPa) and has compensating compressive stress along the exterior (min ≈ -580 MPa). The section release stress change when sectioning the nickel disk forging specimen into a half

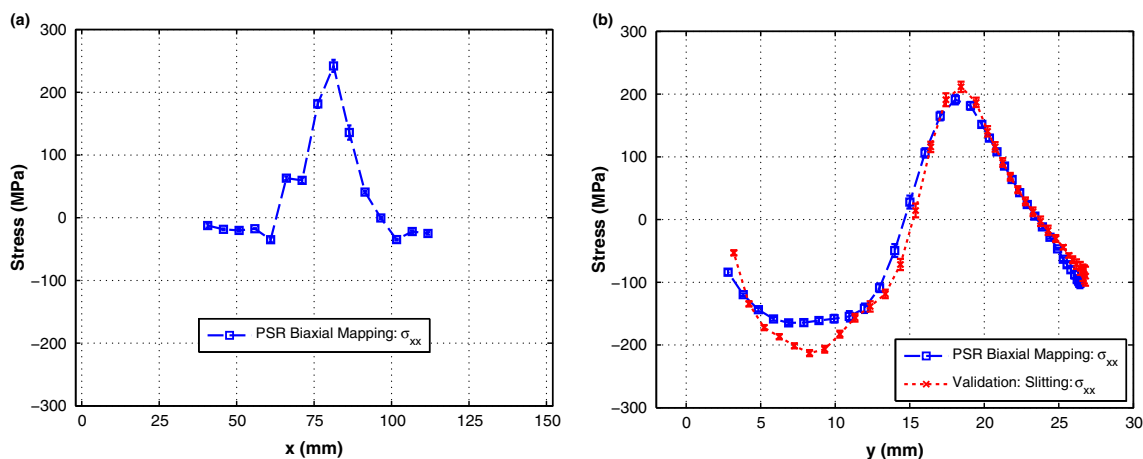


Fig. 12 Line plots of the PSR mapping and a validation slitting measurement for the stainless steel DM welded specimens along the (a) x-direction at $y = 19.05$ mm and (b) along the y-direction at $x = 76.2$ mm

disk has tensile stress at the ID (550 MPa) and compressive stress at the OD (−200 MPa) (Fig. 17(b)).

The total stress and uncertainty maps are shown in Fig. 18. The hoop stress (σ_{zz}) is tensile towards the center of the forging inner diameter (max ≈ 450 MPa) and has compensating compressive stress towards the forging outer diameter and along the top and bottom of the forging (min ≈ -580 MPa). Both the slice and PSR stress significantly contribute to the total radial stress (σ_{xx}), which has tensile residual stress toward the forging center (200 MPa)

and compressive stress at the top and bottom of the forging (−200 MPa). The radial stress uncertainty is low at most points, but is significant at the top and bottom of the forging at $x = 25$ and 30 mm, with the largest uncertainties near 50 MPa.

The stress and uncertainty from the validation contour measurements are shown Figs. 19 and 20. Both measurements show similar trends with tensile stress towards the center of the forging (200 MPa) and compressive stress along the exterior boundary (−200 MPa). The uncertainty in both cases is

Fig. 13 Measured x-direction (a) stress in a thin slice and (b) PSR stress for the titanium EB welded plate specimen Note: Sub-figures use different color scales

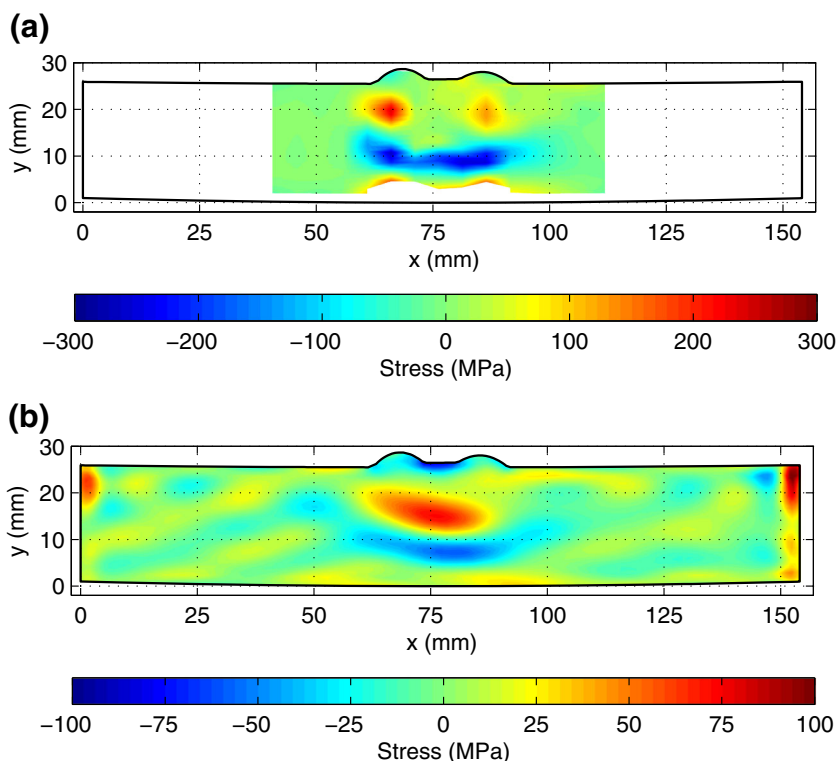
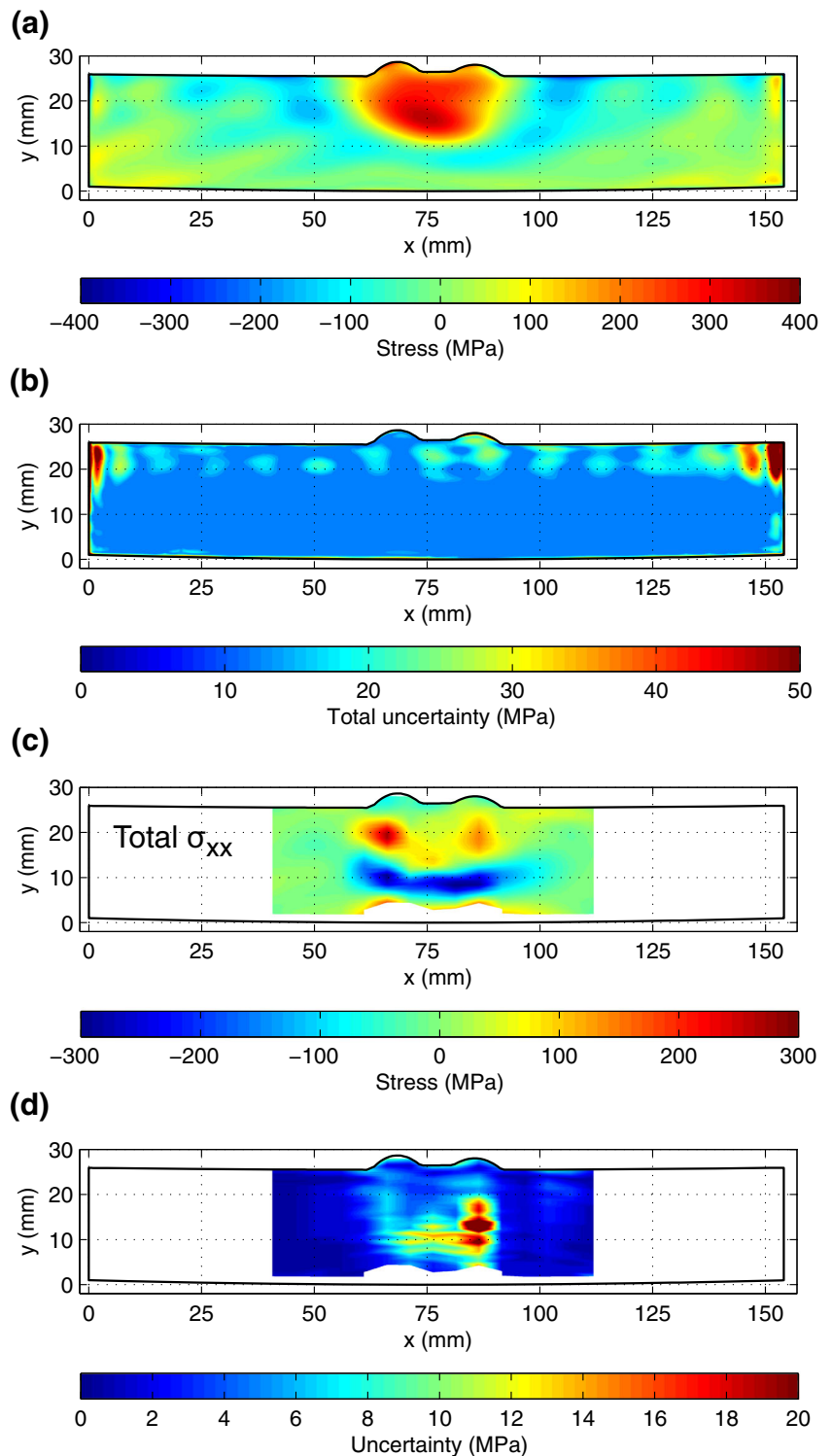


Fig. 14 Stress and uncertainty for the titanium EB welded plate specimen: (a) z-direction stress, (b) z-direction uncertainty, (c) x-direction stress, and (d) x-direction uncertainty. Note: Sub-figures use different color scales



similar, with most values being between an 8 MPa floor and 25 MPa, with larger uncertainties near the exterior boundary (up to 75 MPa).

The comparison between the validation measurements and the PSR mapping results is shown in the line plots of Fig. 21. There is excellent agreement between the

measurements, with values within 15 MPa at most points. The most significant difference occurs for y greater than 35 mm at $x = 27.33$ mm. However, the PSR mapping has an oscillating stress field between $y = 60$ and 70 mm, where the PSR measurement has lower magnitude stress than the validation measurement at $y = 60$ mm and

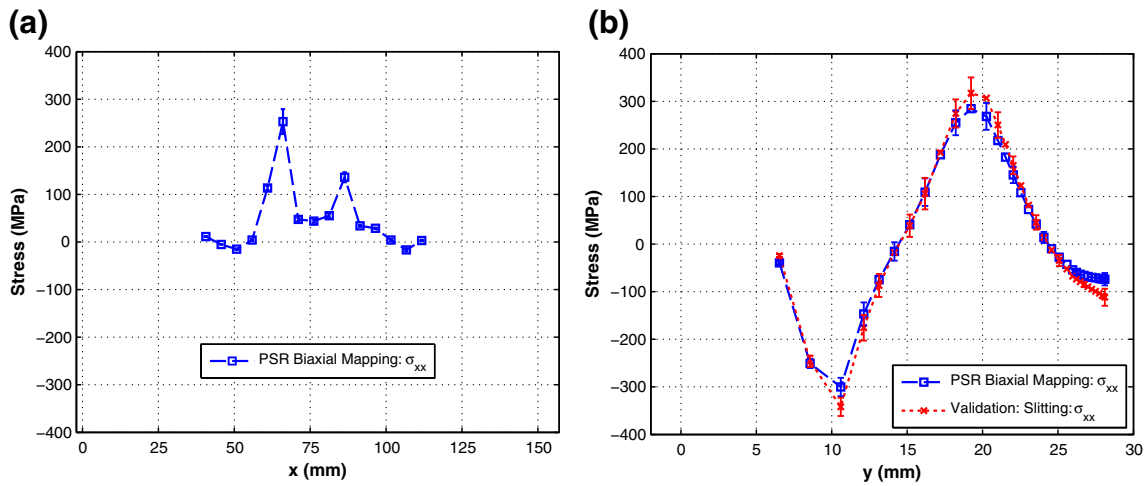


Fig. 15 Line plots of the PSR mapping and a validation slitting measurement for the titanium EB welded plate specimens along the (a) x-direction at $y = 20.32$ mm and (b) along the y-direction at $x = 68.15$ mm

alternatively the PSR measurement shows higher magnitude stress than the validation measurement at $y = 65$ mm (although the measured stresses are within 65 MPa over this region).

Discussion

Each of the four PSR measurements had good agreement with their associated validation measurements, with differences

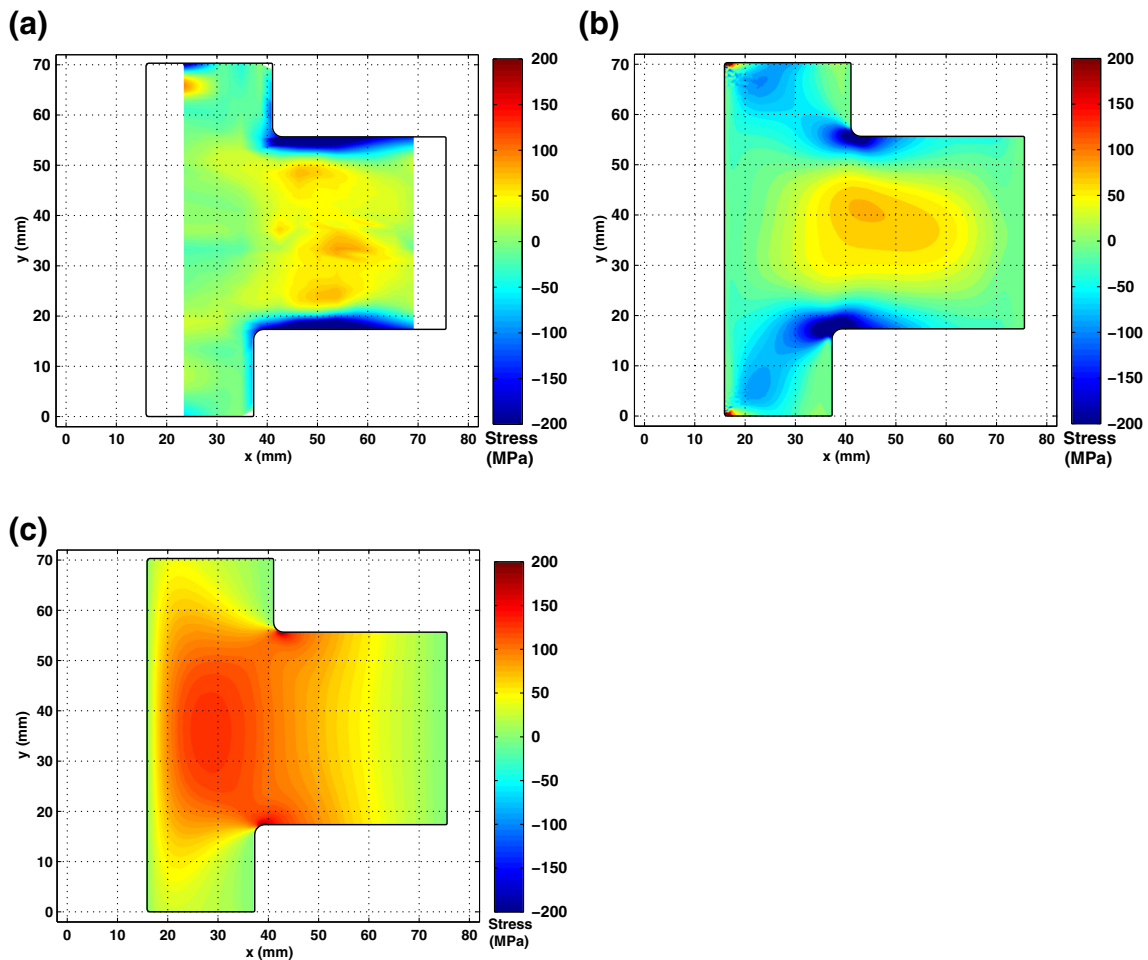


Fig. 16 Measured x-direction (a) stress in a thin slice, (b) PSR stress, and (c) section release stress when sectioning the nickel disk forging specimen into a half disk

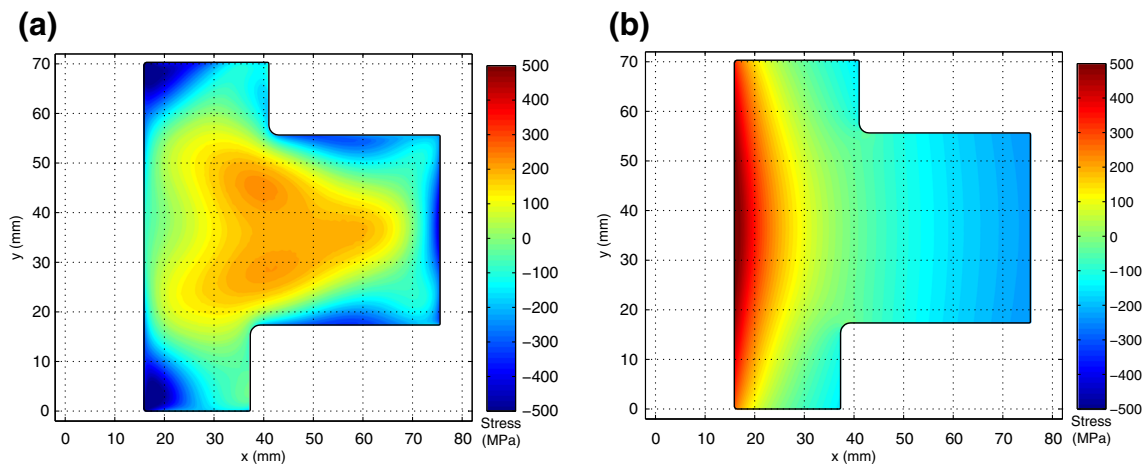


Fig. 17 Measured z-direction (a) contour method stress in the half disk and (b) section release stress when sectioning the nickel disk forging specimen into a half disk

between the measurements relatively small. In the T-section, there was statistical agreement at all points. There was a peak difference of 40 MPa for the stainless steel DM welded plate (8% of the stress range), a peak difference of 40 MPa for the titanium electron beam welded plate (7% of the stress range),

and a peak difference of 65 MPa (8% of the stress range) for the nickel forging. To provide context to these differences between the PSR biaxial mapping measurements and their associated validation measurements, we compare them to differences reported in earlier published studies.

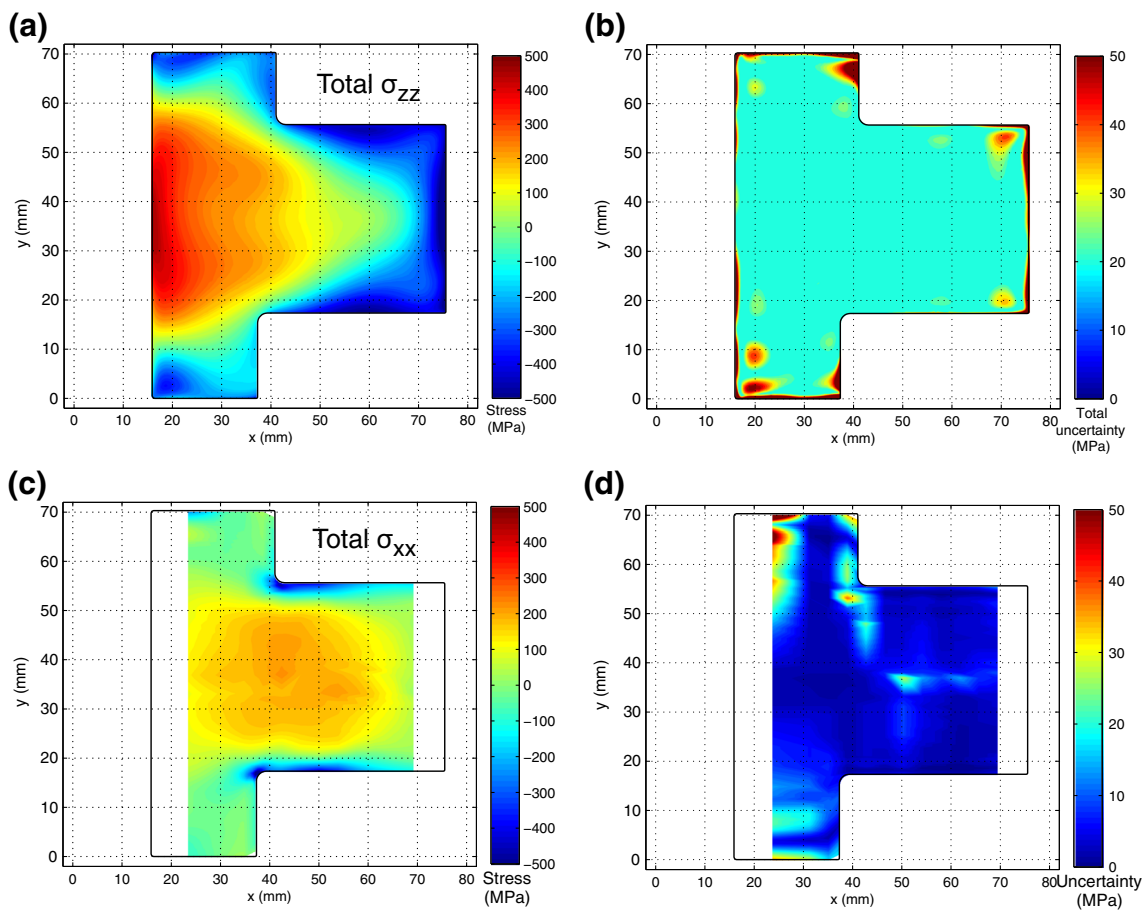


Fig. 18 Stress and uncertainty for the nickel disk forging specimen: (a) z-direction stress, (b) z-direction uncertainty, (c) x-direction stress, and (d) x-direction uncertainty

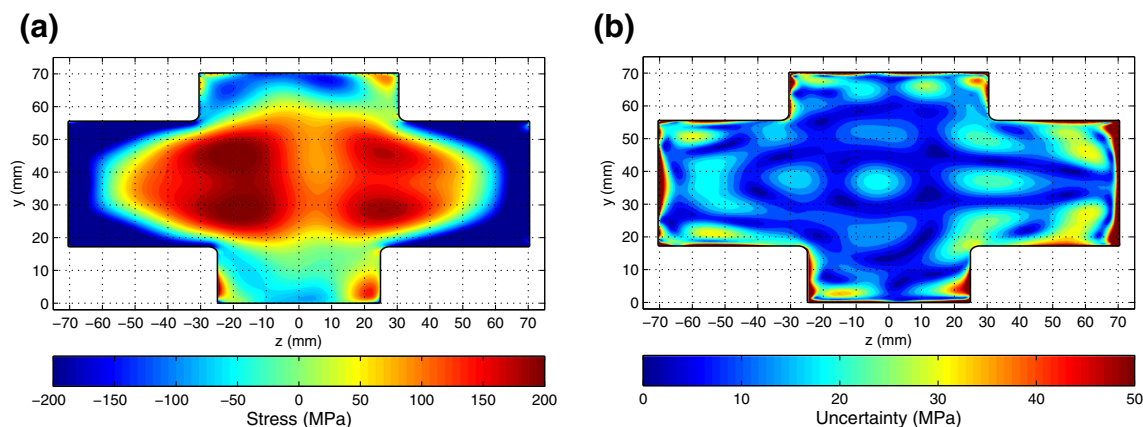


Fig. 19 Measured x-direction (a) stress and (b) uncertainty in the nickel disk forging specimen at $z = 27.33$ mm

Prime, et al. made measurements in a friction stir welded aluminum sample with both the contour method and neutron diffraction [26]. The measured stress had a very low stress range for a weldment, ranging from -30 MPa to 32 MPa. The agreement between the two measurement techniques was good, but had peak differences of 40 MPa ($\sim 65\%$ of the stress range).

Another study performed contour method measurements and neutron diffraction measurements in additively manufactured 316 stainless steel samples made with the laser engineered net shaping (LENS®) fabrication technique [27]. The measured stress had high magnitude, ranging from -300 MPa to 400 MPa. The two measurement techniques had peak differences around 200 MPa (28% of the stress range).

The seminal work by Pagliaro [3], regarding mapping multiple stress components, measured stress in an indented aluminum alloy 2024-T351 disk. Measurements were made using the contour method, neutron diffraction, hole drilling, and x-ray diffraction. The measured stresses had moderate magnitudes, ranging from -120 MPa to 30 MPa. The peak differences between measurement techniques was around 70 MPa,

or 45% of the stress range, but the agreement was within ± 10 MPa at most locations.

Another study performed contour method measurements, slitting, and synchrotron x-ray diffraction measurements in a AISI Type 316H austenitic stainless steel with an autogenously weld along one edge [28]. The measured stress had high magnitude, ranging from -180 MPa to 300 MPa. Results from different techniques agreed at most points within ± 50 MPa and peak difference was around 120 MPa (25% of the stress range).

Considering the measurements in the literature, the differences between the PSR mapping measurements and their associated validation measurements are similar to or better than those found in prior work, where differences were less than 10% of the stress range for all specimens. This level of agreement lends confidence to the PSR biaxial mapping approach. The breadth of specimens used here shows that PSR biaxial mapping is useful for a range of industrially relevant alloys, geometries, and stress states.

The measurement results in the T-section show that, even though most of the material has been removed from the quenched parent bar, a significant amount of residual stress

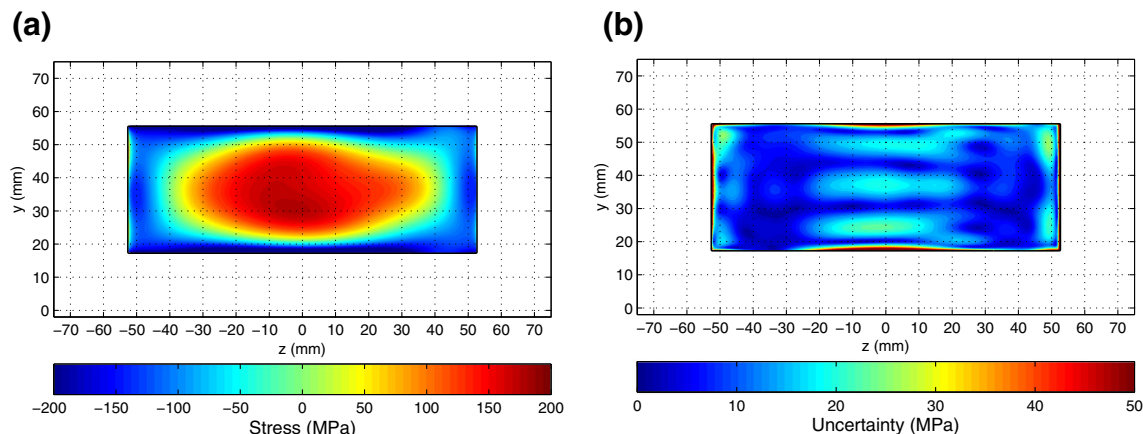


Fig. 20 Measured x-direction (a) stress and (b) uncertainty in the nickel disk forging specimen at $z = 54.0$ mm

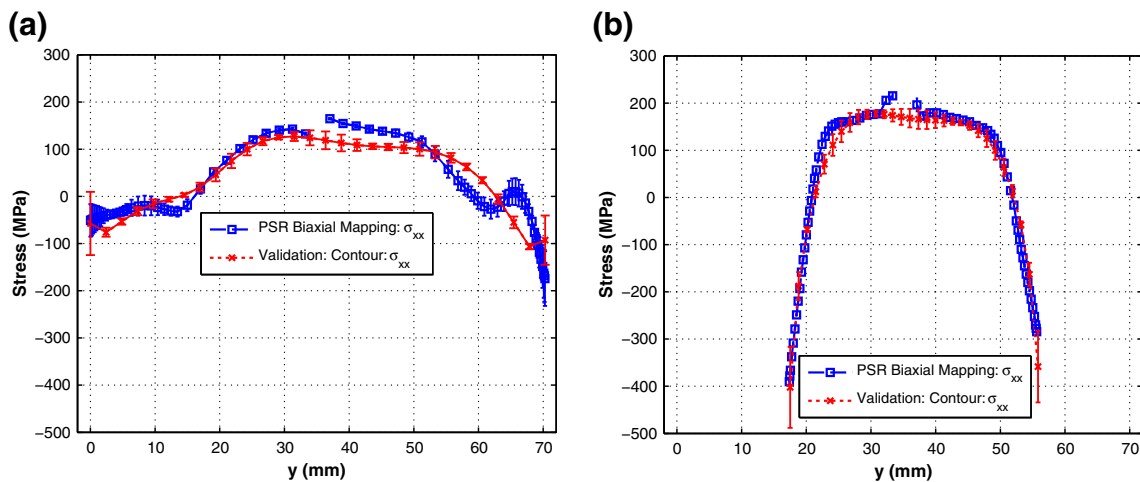


Fig. 21 Line plots of the PSR mapping and validation contour measurements for the nickel disk forging specimen along the y -direction at (a) $x = 27.33$ mm and (b) $x = 54$ mm

remains in the final machined T-section. This phenomenon is especially important for thin-walled aerospace parts that are machined from forged monolithic preforms [29–31], as well as for thin blades machined from a nickel disk preform, since redistribution of residual stresses during machining can cause significant distortion [32–34].

It is interesting that both the stainless steel DM welded plate and the titanium EB welded plate have similar magnitudes and distributions of residual stress, because it shows that specific welding procedures and materials have limited effect on the shape and magnitude of residual stress fields when the specimen geometry and welding geometry are similar.

The measurement in the stainless steel DM welded plate was very similar to a different measurement reported in [13]. Both specimens used identical stainless steel parent plates, weld groove geometry, and weld bead geometry (nominally), but the specimen in [13] had a stainless steel weld metal while the current specimen had a nickel based dissimilar metal weld. Although the weld material was different between these two specimens, both had similar residual stress fields.

Summary/Conclusions

Four PSR mapping measurements were performed using an aluminum T-section, a stainless steel plate with a dissimilar metal slot-filled weld, a titanium plate with an electron beam slot-filled weld, and a nickel disk forging. Each PSR mapping measurement consisted of a contour method measurement to determine one stress component (out-of-plane stress), removal of multiple slices, and measuring one (or two) components of the remaining in-plane stress in the slices. The total stress for the in-plane direction(s) was the combination of the PSR stress and the stress remaining in the slice. Each measurement had a

corresponding validation measurement that confirmed the in-plane total PSR mapping stress. The good agreement between the PSR mapping measurements and validation measurements shows PSR mapping is a viable measurement technique for a wide range of specimen types and engineering applications.

Acknowledgements The authors acknowledge, with gratitude, the U.S. Air Force for providing financial support for this work (contract FA8650-14-C-5026). We would also like to acknowledge Steve McCracken from the Electric Power Research Institute for supplying and fabricating the stainless steel plate with a dissimilar metal slot-filled weld, Brian Streich from Honeywell for providing the nickel forgings, and Andrew Mugnaini from Sciaky for fabricating the titanium samples. Special acknowledgement to Jeffrey Bunn, Paris Cornwell, and Andrew Payzant from Oak Ridge National Laboratory for their help with the neutron diffraction measurements.

A portion of this research was performed at ORNL's High Flux Isotope Reactor and was sponsored by the Scientific User Facilities Division, Office of Basic Energy Sciences, US Department of Energy (proposal IPTS 14081.1).

References

1. Prime MB, Steinzig ML (2014) Beyond the streetlight effect: a united future for relaxation and diffraction methods for residual stress measurement. *Adv Mater Res* 996:234–242
2. Prime MB (2001) Cross-sectional mapping of residual stresses by measuring the surface contour after a cut. *J Eng Mater Technol* 123(2):162–168
3. Pagliaro P et al (2011) Measuring inaccessible residual stresses using multiple methods and superposition. *Exp Mech* 51(7): 1123–1134
4. Hosseinzadeh F, Bouchard PJ (2013) Mapping multiple components of the residual stress tensor in a large P91 steel pipe girth weld using a single contour cut. *Exp Mech* 53(2):171–181
5. Pagliaro P, Prime MB, Swenson H, Zuccarello B (2010) Measuring multiple residual stress components using the contour method and multiple cuts. *Exp Mech* 50(2):187–294

6. Pagliaro P et al (2008) Mapping multiple residual stress components using the contour method and superposition. In: ICRES-8 international conference on residual stresses, vol 52. pp 1–8
7. Pagliaro P, Prime MB, Clausen B, Lovato ML, Zuccarello B (2009) Known residual stress specimens using opposed indentation. *J Eng Mater Technol* 131(3):031002
8. Pagliaro P, Prime MB, Zuccarello B, Clausen B, Watkins TR (2007) Validation specimen for contour method extension to multiple residual stress components. *Experimental analysis of Nano and Engineering Materials and Structures* 635–636. https://doi.org/10.1007/978-1-4020-6239-1_315
9. Olson MD, Hill MR (2015) A new mechanical method for biaxial residual stress mapping. *Exp Mech* 55(6):1139–1150
10. Prime MB, Hill MR (Apr. 2006) Uncertainty, model error, and order selection for series-expanded, residual-stress inverse solutions. *J Eng Mater Technol* 128(2):175–185
11. Lee MJ, Hill MR (2007) Intralaboratory repeatability of residual stress determined by the slitting method. *Exp Mech* 47(6):745–752
12. Kotobi M, Honarpisheh M (2016) Uncertainty analysis of residual stresses measured by slitting method in equal-channel angular rolled Al-1060 strips. *J Strain Anal Eng Des* 52(2):83–92. <https://doi.org/10.1177/0309324716682124>
13. Olson MD, Hill MR, Patel VI, Muránsky O, Sisneros T (2015) Measured biaxial residual stress maps in a stainless steel weld. *J Nuc Eng Rad Sci* 1(4):1–11
14. Hill MR, Olson MD, DeWald AT (2016) Biaxial residual stress mapping for a dissimilar metal welded nozzle. *J Press Vessel Technol* 138(1):011404
15. Olson MD, Robinson JS, Wimpory RC, Hill MR (2016) Characterisation of residual stresses in heat treated, high strength aluminium alloy extrusions. *Mater Sci Technol* 32(14):1427–1438
16. Hill MR, Olson MD, DeWald AT (2014) Biaxial residual stress mapping for a dissimilar metal welded nozzle. In: ASME 2014 pressure vessels & piping division conference
17. Prime MB, DeWald AT (2013) The contour method. In: Schajer GS (ed) *Practical residual stress measurement methods*, Ch 5. Wiley, West Sussex, pp 109–138
18. Schajer GS, Prime MB (2006) Use of inverse solutions for residual stress measurements. *J Eng Mater Technol* 128:375
19. Hill MR (2013) The slitting method. In: Schajer GS (ed) *Practical residual stress measurement methods*. Wiley, West Sussex, pp 89–108
20. Olson MD, DeWald AT, Hill MR, Prime MB (2014) Estimation of uncertainty for contour method residual stress measurements. *Exp Mech* 55(3):577–585
21. Olson MD, DeWald AT, Hill MR (2018) Validation of a contour method single-measurement uncertainty estimator. *Exp Mech* 58:767–781. <https://doi.org/10.1007/s11340-018-0385-4>
22. SAE Aerospace (2006) Aerospace material specification 4342: aluminum alloy extrusions: solution heat treated, stress relieved, straightened, and overaged. 400 Commonwealth Drive, Warrendale, PA 15096, USA: SAE Aerospace; 2006. Report No.: 4342
23. Wong W, Hill MR (2013) Superposition and destructive residual stress measurements. *Exp Mech* 53(3):339–344
24. ISO (2005) Non-destructive testing - standard test method for determining residual stresses by neutron diffraction. International organization for standardization, ISO/TS 21432
25. Coleman HW, Steele WG (2009) In *Experimentation, Validation, and Uncertainty Analysis for Engineers*, 3rd edn. Wiley, Hoboken
26. Prime MB, Gnäupel-Herold T, Baumann JA, Lederich RJ, Bowden DM, Sebring RJ (2006) Residual stress measurements in a thick, dissimilar aluminum alloy friction stir weld. *Acta Mater* 54(15):4013–4021
27. Rangaswamy P et al (2005) Residual stresses in LENS® components using neutron diffraction and contour method. *Mater Sci Eng A* 399(1–2):72–83
28. Hosseinzadeh F, Toparli MB, Bouchard PJ (2012) Slitting and contour method residual stress measurements in an edge welded beam. *J Press Vessel Technol* 134(1):011402
29. Chantzis D, Van-der-Veen S, Zettler J, Sim WM (2013) An industrial workflow to minimise part distortion for machining of large monolithic components in aerospace industry. *Procedia CIRP* 8:281–286
30. Sim WM (2011) Residual stress engineering in manufacture of aerospace structural parts. *Proceedings of 3rd international conference on distortion engineering*. Bremen, Germany, pp 187–194
31. Li J-G, Wang S-Q (2017) Distortion caused by residual stresses in machining aeronautical aluminum alloy parts: recent advances. *Int J Adv Manuf Technol* 89:997–1012
32. Masoudi S, Amini S, Saeidi E, Eslami-Chalander H (2015) Effect of machining-induced residual stress on the distortion of thin-walled parts. *Int J Adv Manuf Technol* 76(1):597–608
33. Wang Z-J, Chen W-Y, Zhang Y-D, Chen Z-T, Liu Q (2005) Study on the machining distortion of thin-walled part caused by redistribution of residual stress. *Chin J Aeronaut* 18(2):175–179
34. Garcia DR, Hill MR, Aurich JC, Linke BS (2017) Characterization of machining distortion due to residual stresses in quenched aluminum. In: *Proceedings of the ASME 2017 12th international manufacturing science and engineering conference*, Los Angeles, CA, USA